Daniel Kiener[a,b,d], Christian Motz[b], Gerhard Dehm[b,c], Reinhard Pippan[b]

[a] Materials Center Leoben, Forschungs GmbH, Leoben, Austria
[b] Erich Schmid Institute of Material Science, Austrian Academy of Sciences, Leoben, Austria
[c] Department of Materials Physics, Montanuniversität Leoben, Leoben, Austria
[d] now at: National Center for Electron Microscopy, Lawrence Berkeley National Laboratory, Berkeley, U.S.A.

Overview on established and novel FIB based miniaturized mechanical testing using in-situ SEM

Dedicated to Professor Dr. Franz Jeglitsch on the occasion of his 75th birthday

Probing mechanical properties in the micrometer regime is of current interest in materials science. A focused ion beam microscope was employed to fabricate miniaturized specimens, while an indenter installed in a scanning electron microscope was utilized to actuate the samples and record the load and displacement data during the deformation. Examples for miniaturized compression, tension, bending, as well as newly developed bending fatigue and bending fracture experiments are presented, demonstrating the unique flexibility of in-situ mechanical testing in the scanning electron microscope at small length scales.

Keywords: Size-effect; Micro-mechanical testing; Focussed ion beam (FIB); in-situ SEM

Introduction

It is common knowledge that the strength of a polycrystalline bulk sample is governed by its smallest microstructural dimension [1–3]. With the still ongoing trend of miniaturization, new methods for testing materials with smaller and smaller dimensions down to the micrometer regime have been developed. Classical work on bending of thin polycrystalline Ni foils [4], torsion of polycrystalline Cu wires [5], and indentation testing [6, 7] shows that there are distinct size effects on the mechanical properties in this size regime. Some of these approaches were even further developed to probe features in the nanometer size regime, for example dedicated micro-electro-mechanical system (MEMS) devices to test free-standing nanostructured thin films in tension [8], or instrumented in-situ indentation in a transmission electron microscope (TEM) to investigate incipient plasticity [9]. While bending [4], torsion [5], and the MEMS [8] techniques were successfully applied to polycrystalline samples, the fabrication of suitable samples imposed limitations to these approaches when aiming to determine the mechanical properties of free-standing micrometer sized single crystals. As a matter of fact, melt cast single crystals cannot be directly fabricated in the shape of a sheet or wire with micrometer dimensions. Nanoindentation techniques provide the resolution of probing quasi single crystal properties in the nanometer regime in polycrystalline material [10], but the complex stress–strain state beneath the indenter complicates the data evaluation. Single crystal thin films can be produced to thicknesses of several micrometers and the effect of the confining substrate can be minimized by newly developed transfer techniques [11]. Still, only one dimension of these films is in the micrometer regime, while the other two dimensions are in the millimeter range.

These fabrication limitations were overcome by the broader availability of focused ion beam (FIB) microscopes in materials science [12]. Using a FIB for local material removal and a flat ended diamond tip for compression testing in a nanoindenter, Uchic et al. [13, 14] were the first to test FIB micro-structured single crystal specimens with all dimensions in the micrometer regime. While their results showed an interesting size effect of increasing strength with reduced sample dimension, which is still a hot topic in the materials science community debate, they also opened up the field to FIB-based micromechanical testing [15]. A number of groups more or less closely mimicked their micro-compression approach and applied it to various materials [16–26], but other loading techniques were also developed, inspired by their work. For example, there were methods developed for micro-bending [27] and micro-tensile testing [28] of miniaturized single crystals. The aim of this overview is to focus on newly developed micro-mechanical test methods rather than discussing size-effects in materials. However, before reporting on novel miniaturized testing concepts a short review of the current understanding of micro-compression testing of single-crystalline face centered cubic (fcc) metals is provided, and challenges and limitations of micro-mechanical testing with a focus on micro-compression testing are discussed.

2. Common observations and challenges in micro-compression testing

2.1. Common observations for fcc single crystals

One of the striking observations of the micro-compression experiments carried out by Uchic et al. [13, 14] was the intermittency of the plastic flow. In load controlled experiments, discrete strain bursts connected by regimes of nearly elastic loading were observed. Exemplary data provided by Frick et al. [29] for Ni(111) showing this behavior is presented in Fig. 1a. The strain bursts are usually interpreted as dislocation avalanches [30, 31], and statistical analysis of the size and frequency of these bursts shows a power law scaling [30, 31]. Apparently, once a dislocation source is activated at a certain stress level, significant plastic deformation can be achieved by easy slip. There seems to be literally no hard-

© 2009 Carl Hanser Verlag, Munich, Germany www.ijmr.de Not for use in internet or intranet sites. Not for electronic distribution.

ening involved, until this source is shut down. At this point the system is loaded in a nearly elastic manner until another source is activated at higher stress levels.

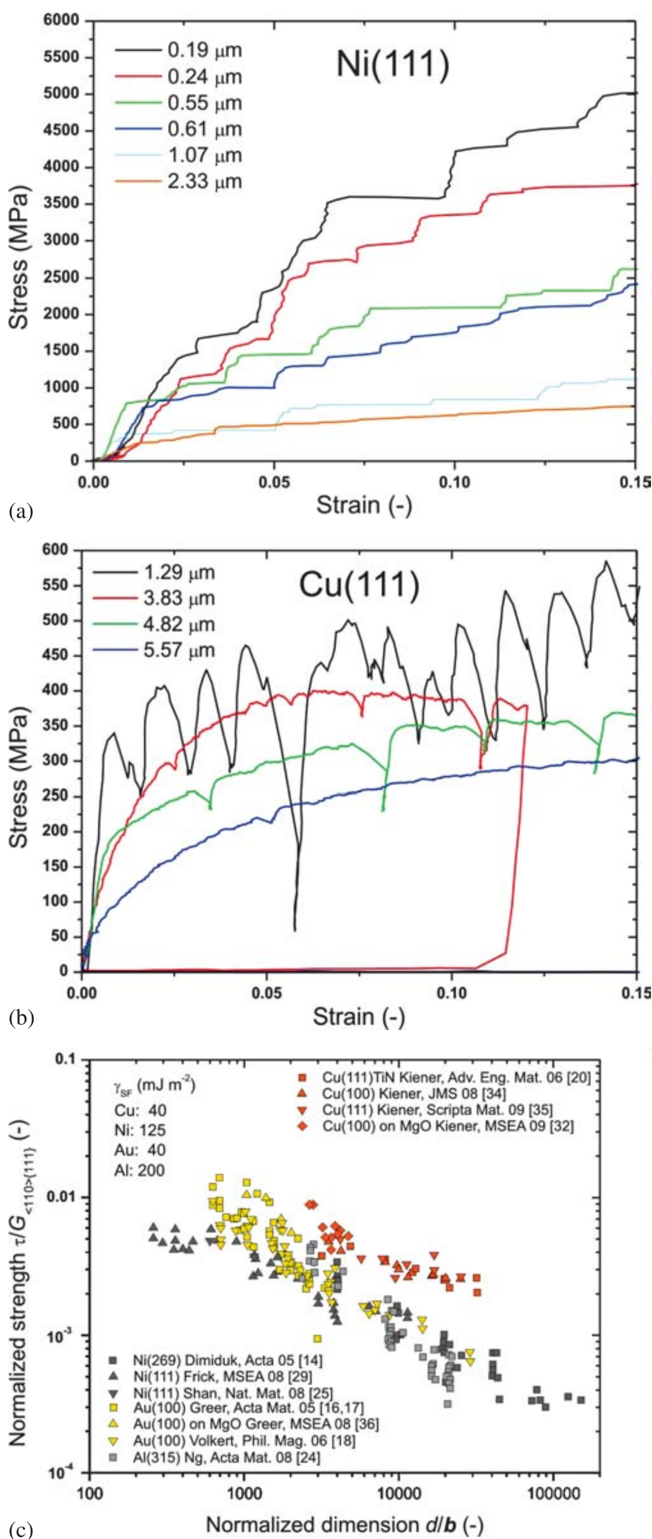

Fig. 1. Common features observed in micro-compression testing of face centered cubic (fcc) materials produced by FIB machining. (a) Ni(111) micro-compression samples of various size tested under load control show discrete strain bursts (redrawn from Frick et al. [29]). (b) Cu(111) samples loaded in displacement control mode depict load drops (redrawn from [20, 32]). (c) Normalized plot of strength versus dimension for micro-compression results obtained from various fcc metals [14, 16–18, 20, 24, 25, 29, 32, 34–36]. In general higher strength is observed for smaller samples.

In displacement controlled testing, the occurrence of load drops is observed. Once a source is activated, it will emit dislocations and thereby generate strain. These dislocations move faster than the usual strain rate of such a quasi-static experiment. This results in a reduction in the contact force seen as a vertical drop in the load–displacement data. When the displacement rate controlled flat punch catches up with the sample, it will be reloaded in a close to elastic manner. An example of this behavior is shown in Fig. 1b [20, 32] for Cu(111) micro-compression samples. Therefore, strain bursts and load drops are generally regarded as equivalent. However, a frequently overlooked but significant difference between the two loading modes can be rationalized when looking at the stress–strain curve of the smallest sample (diameter 1.29 μm) shown in Fig. 1b. There are several minor load drops that occur at lower stresses than the previous major load drop. This cannot be observed in load controlled mode, where the load would stay at the level of the previous major burst [33].

A second important observation by Uchic et al. [13, 14] was the inverse scaling of strength with sample size. This has been widely confirmed in various micro-compression studies and is also obvious from the data shown in Fig. 1a and b. A more comprehensive dataset for Cu [20, 32, 34, 35], Ni [14, 25, 29], Au [16, 18, 36], and Al [24] is shown in Fig. 1c. To compare the different materials in an intuitive dimensionless plot, as very recently suggested by Dou and Derby [37], the shear strength τ was normalized by the anisotropic shear modulus $\boldsymbol{G}$ and the sample dimension d by the Burgers vector $\boldsymbol{b}$. Note that the studies differ in the representative strain used to determine the flow stress level, ranging from the plastic limit [24] to 10% strain [16, 32]. Nevertheless, a size effect is observed in all cases. This is generally rationalized by a scaling of the dislocation source size with the sample size, causing higher stresses for smaller samples [28, 38–42]. Values of a power law fitting to the data range between $d^{-0.4}$ and d^{-1}. The power law exponent itself is influenced by several experimental factors, for example the initial dislocation density [43] and strain rate [44], as well as details of the data evaluation, for example the representative strain value used to determine flow stresses [45] and the fitting method [46].

Similar observations in terms of strength scaling, intermittency and stochastic flow, but with differences in the hardening behavior and the scaling exponents, are also observed in body centered cubic (bcc) materials. A detailed treatment is beyond the scope of this article, the interested reader is referred for example to a recent review [47].

2.2. Need for in-situ experiments

An important and frequently discussed issue in any small scale testing is the alignment between sample and testing equipment [48, 49]. There are ways to improve alignment issues ex-situ [15], but clearly the benefits from performing measurements in-situ is that, beside minimizing these alignment issues, direct visual control of the experiment significantly increases the reliability of information gained during a mechanical test. Ex-situ testing relies on linking of the specimen characteristics prior to testing and after ex-situ characterization by the measured mechanical data. This can be done for continuous and homogenous sample defor-

© 2009 Carl Hanser Verlag, Munich, Germany www.ijmr.de Not for use in internet or intranet sites. Not for electronic distribution.

© 2009 Carl Hanser Verlag, Munich, Germany www.ijmr.de Not for use in internet or intranet sites. Not for electronic distribution.

mation, comparable to what is known from bulk testing. With increasing complexity of the deformation behavior, even the simple question for the true stress can be a matter for discussion, since for example the actual minimal sample cross-section or the contact area are unknown. This is easily rationalized for micrometer sized single crystal samples that deform by dislocation glide, given the stochastic [24] and discrete nature [31] of deformation on this length scale. For amorphous materials these geometrical problems are also of major concern. A recent analysis showed that the postulated size effect in the deformation of micrometer sized amorphous compression samples could be to a large extent caused by an improper estimation of the contact size [26]. The above clearly shows that the issues mentioned are in general geometrical problems, independent of the investigated material. As a consequence, all the samples presented here were tested in-situ in a scanning electron microscope (SEM) to have permanent documentation of at least two of the three sample dimensions.

3. Available in-situ testing setups

There exist several methods for direct in-situ observation in the micrometer regime, using either imaging or X-ray methods. Here we focus on the most general and flexible technique, namely direct visual control in an SEM. Compared to optical microscopy, the SEM offers higher resolution and reduced environmental influences. Meanwhile there is a growing number of groups that have installed an instrumented indenter system in an SEM [20–22, 34, 50–53]. Similar approaches have even been realized in a TEM [8, 9, 25, 54–56], offering higher resolution and the possibility to observe the sample deformation direct or in diffraction mode [42, 57]. A drawback of the TEM approach is the limited thickness to maintain electron transparency of the investigated material. Concerning the X-ray methods, micro-Laue techniques were applied to characterize the sample microstructure in the initial state for Si, Au, Ni, Cu and NiTi samples in [19, 58] and in-situ during the experiment for Au and Cu samples in [59, 60], while micro-Raman spectroscopy [61] was used for local in-situ stress measurement of Si samples.

3.1. SEM and attached micro-indenter

The requirements for the SEM to perform micro-mechanical testing are rather moderate. Besides a large vacuum chamber to contain sample and loading equipment, just several flanges with signal feedthroughs for piezo voltage supply as well as load and displacement measurement are required. In the present work, a tungsten filament SEM (Carl Zeiss SMT AG, Oberkochen, Germany; LEO 440 Stereoscan) typically operated at 10–20 keV was used together with a micro-indenter system (ASMEC, Radeberg, Germany; UNAT) for sample loading. To save operational space, the indenter positioning system is partially contained in an attached cap. For this reason, these stages can stay attached to the SEM once the micro-indenter is removed for ex-situ use. Additionally, to improve the signal-to-noise ratio, the whole SEM was put on an active vibration isolation system (Halcyonics, Goettingen, Germany). Figure 2

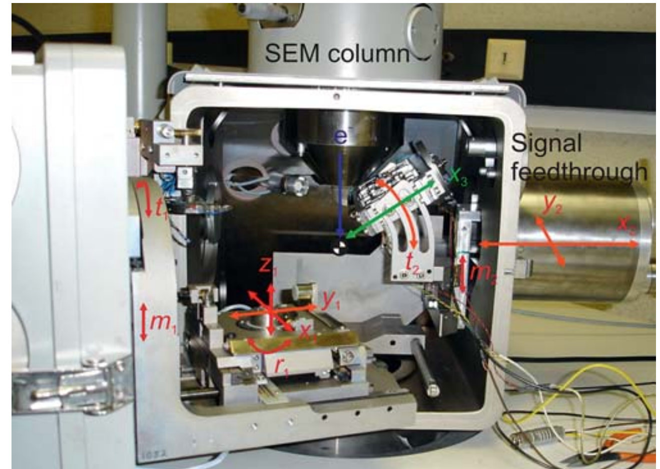

Fig. 2. View into the open SEM chamber with the micro-indenter installed, including indication of the available axis and the coincidence point.

shows the open SEM chamber with the micro-indenter in an inclined position suited for indentation experiments under a predefined (viewing) angle. Note that the sample surface has to be tilted accordingly.

In the following, the purpose of the indicated axis will be briefly explained. On the indenter side, four axes (x_2, y_2, m_2, t_2) allow to position the indenter tip in the electron beam (x_2, y_2) at the desired working distance (m_2) and inclination angle (t_2). Due to constructional limitations given by the SEM column, the minimum working distance is about 10 mm. This mechanical alignment of adjusting the indenter tip in the electron beam is done at moderate magnifications of the order of 1000×. Changing the field of view at higher magnifications during testing is accomplished using the electron beam shift of the SEM.

The sample is moved into the coincidence point using the SEM stages. The linear axes x_1, y_1, z_1, (m_1) are in principle sufficient for positioning. The rotational axis r_1 ensures alignment between indenter loading axis (x_3) and specimen axis (x_1) in the x-direction. The tilting axis t_1 is required to ensure orthogonality between sample surface and indenter loading axis. The actual test is performed with the instrumented x_3 axis of the indenter. A schematic arrangement of the different axis in the aligned system is given in Fig. 3f, while the movement ranges are provided in Table 1.

For all tests presented in this work except of the indentation shown in Fig. 3a and b, samples were situated at edges or freestanding on the tip of needles. In these cases, the indenter can be used in the horizontal position ($t_2 = 0$). This simplifies alignment and reduces uncertainties from an inclined view.

Table 1. Overview of the available axis and their moving range.

SEM		Indenter	
Axis	Range	Axis	Range
x_1	±30 mm	x_2	±5 mm
y_1	±30 mm	y_2	±3 mm
z_1	±4 mm	x_3	±30 µm
m_1	±30 mm	m_2	±25 mm
t_1	−10°–+80°	t_2	0°–25°
r_1	360°		

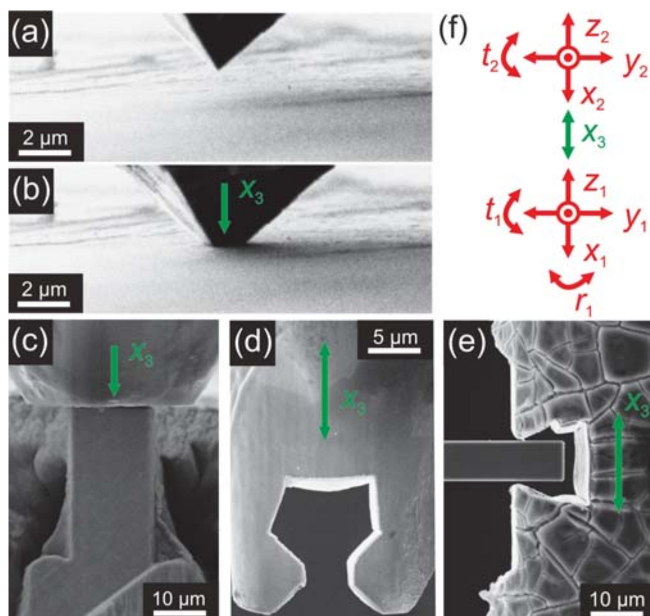

Fig. 3. (a, b) Sharp diamond cube corner tip for indentation, beam bending and bending fracture experiments (not shown here). (c) Flat ended conical 20 μm diamond tip for micro-compression experiments. (d) Custom made tungsten sample gripper for micro-tensile loading. (e) Side slit with wedges for reverse bending and bending fatigue loading. (f) Schematic depicting the available axis of the applied in-situ set-up.

3.2. Indenter tips

Besides commercially available sharp tips (cube corner, Berkovich) used for in-situ indentation (Fig. 3a and b), beam bending, and fracture experiments, there is a variety of custom-made tips. The easiest and most frequently used approach is to flatten a sharp indenter tip by FIB milling to obtain a flat punch of the desired dimensions (Fig. 3c) [13, 15, 20, 62]. Flat punches are also commercial available (e. g. Synton MDP, Nidau, Suisse) [18]. In our lab a large variety of custom and commercial flat punches made of diamond, tungsten or steel with diameters of 2 μm, 8 μm, 10 μm, 20 μm, 50 μm, and 200 μm are available. Choosing the flat punch large enough to cover the whole specimen is important. On the other hand, the smaller the tip, the larger is the view of sight and the less surrounding material needs to be removed by FIB milling to prevent contact of the flat punch and nearby bulk material. Metallic punches reduce charging problems caused by the electron beam, which can become an issue especially when both sample and tip are non-conductive. Changing the contact partners by using flat punches of different materials may even open new possibilities for studying adhesion issues.

In addition to these rather common tips, there are several custom designed tips that also require FIB milling for fabrication. These are for example differently sized micro-grippers dedicated to micro-tensile testing (Fig. 3d) and side-slits with defined wedges for reverse bending and bending fatigue experiments (Fig. 3e).

4. Sample fabrication

Sample fabrication using FIB milling offers a unique technique to shape various materials with a precision of better than tens of nanometers and surface roughness of some nanometers [63]. The general approaches and important parameters as well as the possible material modifications from this milling process will be briefly described. However, the details of FIB fabrication of the individual specimens will not be discussed, as this is beyond the scope of this work.

A FIB (Carl Zeiss SMT AG, Oberkochen, Germany; Zeiss 1540 XB) operated with Ga^+ ions at 30 keV is applied. For coarse milling typical ion currents are of the order of several nA. These are stepwise reduced to final polishing currents of about 0.1 nA. When using perpendicular ion impact for material removal, a higher ion damage can be expected from simulations and experimental studies [63]. Furthermore, perpendicular ion impact in conjunction with the crystal orientation/impinging angle dependent sputter yield [64] leads to a broadening of the milled face with increasing depth [65]. This finally results in unwanted specimen taper as seen in many micro-compression experiments. To circumvent this, lathe milling techniques [15] or other techniques that facilitate grazing ion impact by back-tilting the specimen [20] can be applied. These are, however, more complicated to realize, especially for smaller sample dimensions. For example, Uchic et al. so far used their lathe milling for compression samples with diameters of 1 μm or larger [13, 15].

It was shown recently that the strength of defect free whiskers that sustained stresses close to the theoretical strength in their pristine state [66], was reduced significantly [67] by the presence of artefacts created by FIB milling [63, 68]. In fact, the material behaved as being pre-strained [62], thus containing a higher amount of mobile dislocations than expected for a perfect whisker or a well annealed melt grown single crystal. This is a critical observation when trying to understand the size dependent strength of single crystals in the micrometer regime, since the fabrication technique might artificially alter the dislocation density and as a consequence the mechanical response. Therefore, we will focus on materials that per se contain a higher density of defects, implying that the influence of FIB damage does not play an important role in these cases.

Other limitations of FIB processing are possible formation of new phases [64, 69] or the well documented liquid metal embrittlement. It was for example shown that sub-monolayer wetting of Al grain boundaries by Ga causes embrittlement of these boundaries [70, 71].

Newly developed He^+ ion microscopes are promising for future development of micro sample fabrication. While the much lower milling rates when using He^+ ions will not allow actual sample fabrication, removal of the damaged surface layer caused by Ga^+ ion milling is a very desirable option achievable when using He^+ ion microscopes.

At the same time, alternative fabrication methods are being developed. The main goal here is to reduce the required amount of ion milling or to replace it completely. Moreover, strong parallelization of the sample fabrication process is desirable. Among these emerging methods are micro-electrodischarge machining [15], electroplating [16], photolithography etching techniques [22], directional solidification with subsequent etching [62], and embossing [46].

© 2009 Carl Hanser Verlag, Munich, Germany www.ijmr.de Not for use in internet or intranet sites. Not for electronic distribution.

© 2009 Carl Hanser Verlag, Munich, Germany www.ijmr.de Not for use in internet or intranet sites. Not for electronic distribution.

5. Examples of in-situ deformation techniques in an SEM

In the following exemplary case studies of different in-situ deformation techniques will be provided. No examples for in-situ indentation in an SEM will be shown, since there is extensive literature available [51, 52, 72].

5.1. Compression testing

Compression testing is known to be strongly influenced by boundary conditions, which are difficult to control in micro-compression testing [32]. Nevertheless, there are situations where these limitations are of minor concern and the technique can be applied successfully. This holds true especially if the microstructural dimensions are significantly smaller than a micron-sized compression sample. The other general concern is related to the defects generated during FIB milling. It is reasonable to assume that materials that per se contain a high defect density should not be susceptible to FIB damage [73]. Material systems that fulfil these requirements are, for example, sputter deposited hard coatings with grain sizes of some tens of nanometers [74], or nuclear reactor steels exposed to neutron radiation damage.

The lifetime reduction of a structural steel due to radiation damage is probed by mechanical testing. While real reactor tests are time consuming and expensive, similar material damage can be created by proton irradiation at lower costs and without strongly activating the material. A limitation is given by the low penetration depth of the protons compared to classical neutron irradiation. Thus, small scale testing techniques are required. Indentation testing of the irradiated material reveals an increase in hardness, which can be correlated to an increased yield strength [75, 76]. It is, however, difficult to access important quantities such as the hardening capability, the fracture toughness, or the strain to failure of the irradiated material by indentation techniques. Thus, micro-compression tests of samples situated in individual grains in the irradiated and unirradiated material were performed on FIB fabricated micro-compression samples [77]. Since this complex alloy consists of a martensitic microstructure, the critical dimension is given by the lamellar width, and not the sample dimension itself. The grains were screened with respect to the lamella spacing and grains with lamellae oriented edge-on were selected, but no detailed orientation information was collected. Subsequently, specimens with dimensions of 8 μm × 8 μm × 15 μm were fabricated to sample a volume as large as possible within a single grain. Since the material was on purpose irradiated with a 2 MeV proton beam at doses corresponding to 7 displacements per atom, no influence from FIB damage is expected for the samples tested in the irradiated condition.

The stress versus strain results of four samples FIB fabricated under identical conditions are shown in Fig. 4a. The proton irradiated samples exhibit higher stresses than the unirradiated specimens. While the data of the unirradiated samples are in close agreement, there are differences between the two curves of the irradiated samples. This is expected to result from the grain orientation, which is not known. Taking the derivative of the stress versus strain data, the strain hardening rate was obtained and is depicted in Fig. 4b. There is some scatter in the data which results

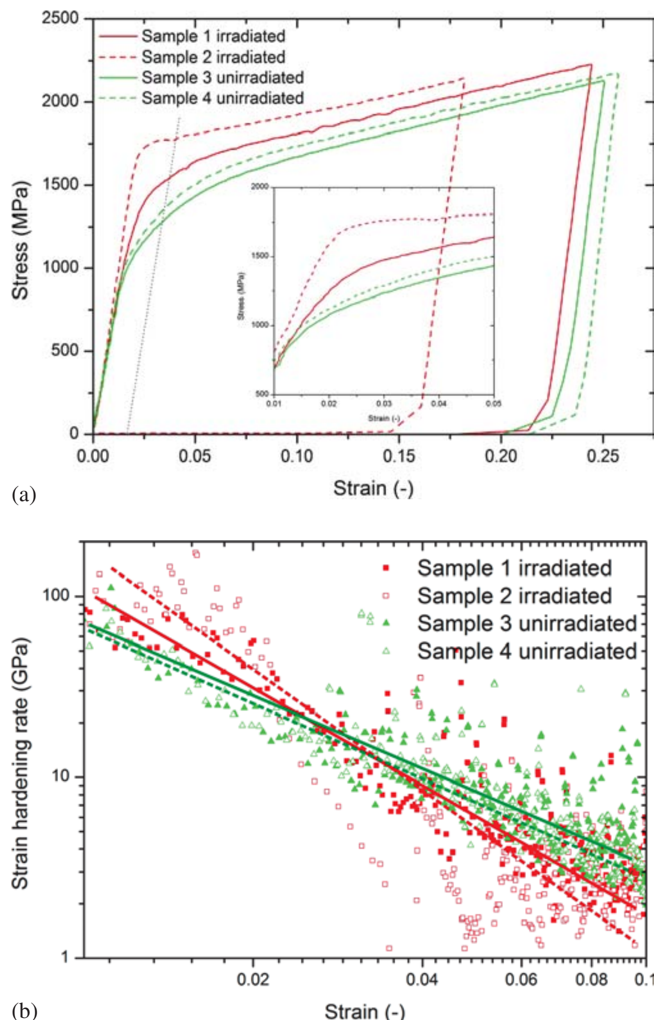

Fig. 4. (a) Stress versus strain curves of 8 μm × 8 μm × 15 μm micro-compression samples situated in single grains in the irradiated (red lines) and unirradiated (green lines) material. Higher yield stresses are observed for the irradiated material [77]. (b) Derivative of the data from (a) showing that the irradiated material has higher initial hardening and less work hardening capability at higher strains compared to the unirradiated material.

from noise in the measurement as well as discrete plasticity events [31] leading to "spikes", since the derivative was taken directly from the measured data without any curve fitting. However, a general trend that the unirradiated material shows lower initial hardening and higher hardening capability at strains above about 3 % is observed.

5.2. Tensile testing

While tensile loading can be difficult to perform on brittle or very hard materials, it is the preferable method to test ductile materials. Here we show another application of a previously developed tensile setup [28]. By FIB fabricating a micro-tensile sample with a specially shaped head and a corresponding individual gripper (Fig. 3d, Fig. 5a), tensile loading can be performed. The result shown here depicts the mechanical behaviour of a nanocrystalline Cu micro-tensile specimen with dimensions of 3 μm × 3 μm × 15 μm and an average grain size of 0.2 μm ± 0.1 μm as produced by severe plastic deformation [78]. Such material is known to possess very high dislocation densities, thus the damage

introduced by FIB milling can be neglected. The sample has no perfectly regular dimensions, because orientation dependent sputter rates [64] lead to the preferential removal of certain grain orientations, resulting in irregular edges. These stress concentrations also pre-define the necking region, as can be seen in the in-situ SEM image at 6.1 % strain (Fig. 5a) as well as recorded with a higher resolution ex-situ in the unloaded condition after having been strained to 6.7 % (Fig. 5b). Nevertheless, comparison between the stress versus strain curve of this micro-tensile test and a macroscopic tensile test with similar microstructure and sample dimensions of 1.2 mm × 1 mm × 8 mm loaded in a commercial tensile machine also suited for in-situ tensile testing in an SEM (Kammrath & Weiss GmbH, Dortmund, Germany) shows close agreement. This is because even for the micro-tensile specimen there are several grains across the sample cross-section and it is the grain size that controls the dislocation generation and motion. For comparison, samples with grain sizes of 100 μm, 10 μm, and 1 μm tested using the tensile stage [79] are also included in Fig. 5c.

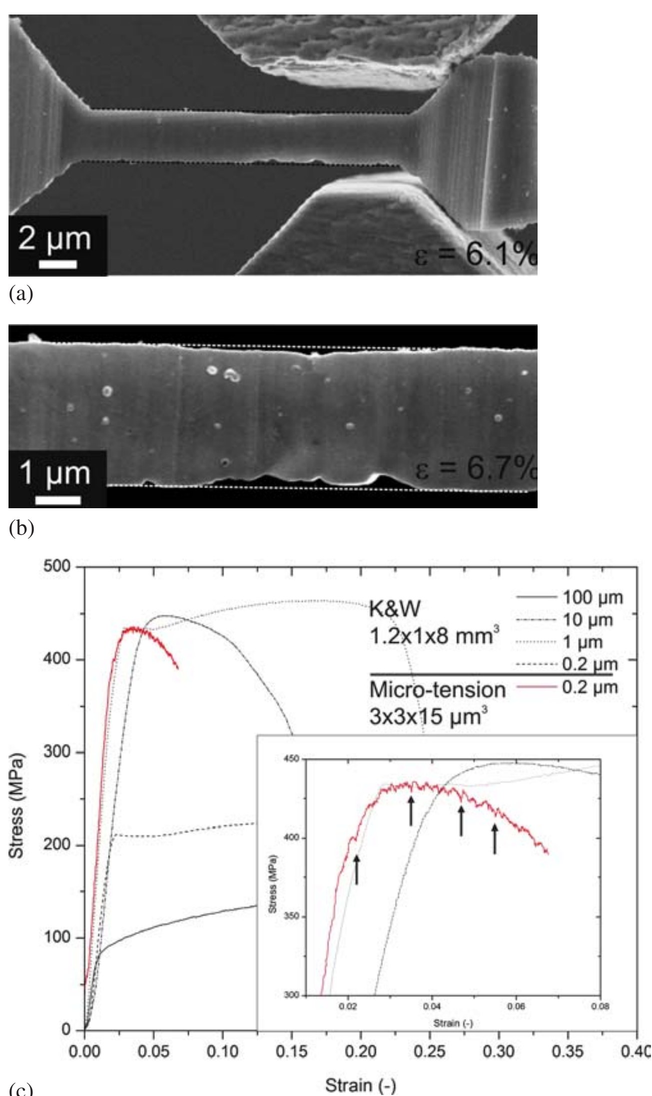

Fig. 5. (a) In-situ SEM image of a Cu micro-tensile specimen with an average grain size of 0.2 μm at a strain of 6.1 %. (b) Ex-situ SEM image of the unloaded sample showing the necking zone at the maximum strain of 6.7 %. (c) Stress versus strain curves of macroscopic Cu samples with grain sizes of 100 μm, 10 μm, 1 μm, and 0.2 μm deformed using a regular tensile machine (black lines) [79] and a Cu micro-tensile specimen with a grain size of 0.2 μm (red line). Close agreement between the macroscopic and the microscopic sample with a grain size of 0.2 μm is observed. The inset shows a detail of the stress versus strain curve, individual load drops indicated by arrows are caused by discrete plastic events.

Compared to the commercial straining stage, where the displacement is measured at the cross-head, it is worth pointing out the very reliable strain determination in the case of the micro-tensile test, where the elongation is measured at the indenter tip. This is shown by the high elastic slope of the micro-tensile test compared to the macroscopic samples. Further improvement is possible by image correlation, as will be discussed in Section 5.1. Another interesting feature is visible in the inset in Fig. 5c. While the measured curve of the macroscopic sample is smooth, the curve of the microscopic sample shows stress drops indicated by arrows. This is typical for dislocation avalanches in displacement controlled tests and can usually only be observed if the sampled volume is small enough [31]. Similar observations with more pronounced load drops were reported for straining of Cu wires with comparable diameter but larger grain size [80, 81].

An alternative method to accomplish tensile loading with a simple indentation setup is depicted in Fig. 6a for a single crystal Cu(100) sample. A ∼3 μm thick lamella is structured to a U-shaped configuration. The bar on the left hand side is further thinned to become the actual tensile specimen with dimensions of 1.5 μm × 1 μm × 5.5 μm, while the right hand side acts as a hinge. Actuating the indenter tip along x_3 bends the structure around the hinge and causes the left hand side to elongate under a tensile stress.

Loading the hinge with a sharp tip causes at the same time indentation of the lamella. This yields additional measured displacement, which has to be corrected for. Figure 6b shows the measured load versus displacement data at the indentation tip (dashed line). Applying the equilibrium of momentum at the hinge, the lower load at the tensile sample was calculated and is given by the dotted line. The actual strain of the tensile specimen was measured in-situ during loading, resulting in the final load versus displacement curve depicted by the solid line in Fig. 6b. Another possibility of correcting for the additional indentation is to subtract the displacement from reference indents made in the same lamella [27]. This approach was performed for the bending experiments explained in the next chapter. The stress versus strain curve presented in Fig. 6c shows a low loading slope compared to the micro-tensile tests shown previously (Fig. 5c). This is presumably because the image resolution is not high enough to clearly discriminate between the indentation displacement and the elongation of the tensile specimen in this initial loading regime. After straining to ∼5 %, a decrease in the technical stress is observed. This is caused by the formation of a single large slip step indicated by an arrow in Fig. 6d. This is not common for a macroscopic multiple slip oriented sample, but has been observed several times for miniaturized specimens and explained by the stochastic nature of dislocation sources in this size regime [82].

The flow stress before necking of ∼350 MPa corresponds to a resolved shear stress of ∼140 MPa. This value is significantly higher than that of ∼50 MPa observed for freestanding Cu micro-tensile specimens of similar dimensions [28]. This indicates that the possible bending component and the limited lateral movement of the bending lamel-

© 2009 Carl Hanser Verlag, Munich, Germany www.ijmr.de Not for use in internet or intranet sites. Not for electronic distribution.

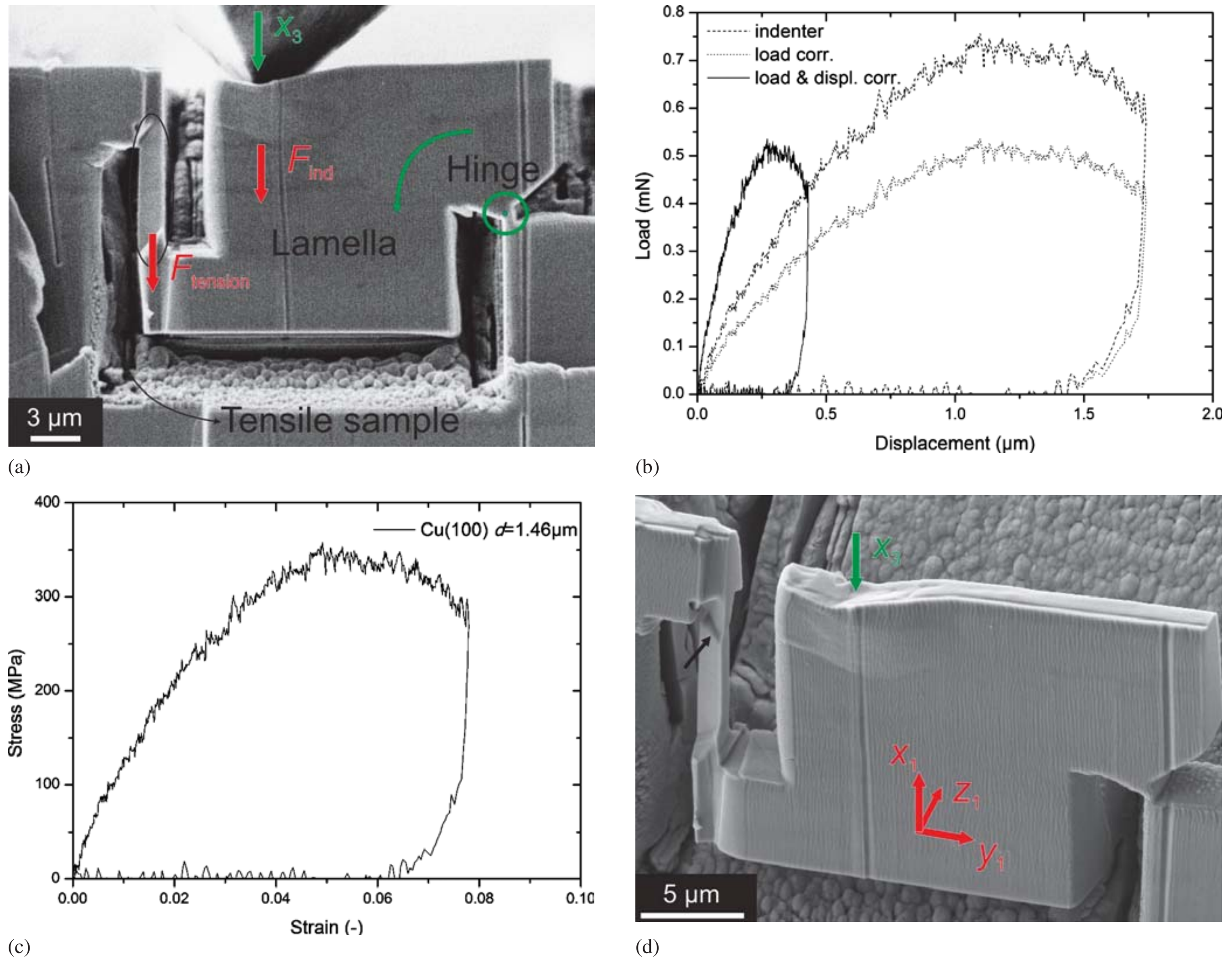

Fig. 6. (a) In-situ tensile test of a 1.46 μm diameter single crystal Cu(100) specimen using a modified bending configuration actuated with a cube corner tip. (b) Measured load versus displacement data (dashed), corrected load at the tensile specimen (dotted), and indentation depth corrected load versus displacement data (solid). (c) Stress versus strain data for the micro-tensile sample calculated from the corrected load versus displacement data (solid line in (b)). See text for details concerning the low slope during loading. (d) Inclined ex-situ SEM image of the sample, showing the formation of one pronounced slip step.

la in the x_1 and z_1 directions by the stiff indenter tip exerts a significant constraint on the deformation of the single crystal specimen, resulting in higher flow stresses as studied in detail for micro-compression and micro-tensile experiments in [35]. However, the limited lateral movement of the miniaturized tensile sample should be of minor influence when testing fine grained materials, where the microstructural dimensions are far below the geometrical specimen dimensions.

The sample design of Fig. 6 requires a noticeable amount of coarse FIB milling to provide enough free space for later fine milling in order to avoid material redeposition and assure precise geometries without any contact between moving parts and redeposited material. Generally, the geometry is more time consuming in fabrication and larger in dimensions compared to the miniaturized tensile sample shown in Fig. 5. An additional drawback is the superimposed indentation and bending process, which makes the data evaluation more tedious.

The advantages are a higher load resolution compared to uniaxial loading, since the contact point of the indenter can be chosen along the lamella. This is a consequence from the equilibrium of momentum around the hinge. Moreover, a symmetric version of this tensile approach can be designed with two tensile specimens instead of one specimen and a hinge. This minimizes possible bending of the tensile samples, but only allows measuring an average strength for both samples. Last but not least, since only a sharp tip needs to be positioned on the lamella, this test can be reasonably performed ex-situ with an indenter system offering imaging possibility by scanning with the tip.

5.3. Beam bending

Bending beams as shown in Fig. 7a have already been used to investigate the influence of strain gradients on the mechanical properties of single crystal Cu in the micrometer regime [20, 27]. Here the results from micro bending tests performed on single crystal W[110](111) samples with thicknesses of 5 μm and 1 μm (Fig. 7a and b) and nanocrystalline Cu specimens with thicknesses of 1.9 μm and 3.9 μm (Fig. 7c and d) are presented. Interestingly, the single crystal W beams show remarkable plasticity, with the dislocation activity being confined to the highly stressed zone

© 2009 Carl Hanser Verlag, Munich, Germany www.ijmr.de Not for use in internet or intranet sites. Not for electronic distribution.

close to the sample base (Fig. 7b). In the case of the nanocrystalline bending beams shown in Fig. 7c and d, no distinct deformation features or differences between the two beams with different thickness can be deduced, although there is a difference in the applied strain gradient. The load versus displacement data of the four tests is presented in Fig. 7e. It was corrected for the additional displacement caused by indentation of the beam. This displacement was taken from reference imprints placed in the base region between the two samples [27]. Note that for the single crystal W[110](111) samples intentional unloading steps were performed.

For a better comparison between the different samples, the data was replotted as normalized bending moment $F \cdot l_B/(w \cdot t^2)$ versus normalized displacement u/l_B in Fig. 7f [27, 83]. Here, F and u are the load and displacement, respectively, while the bending beam is described by the bending length l_B, the width w, and the thickness t. These dimensions are indicated in Fig. 7a and given in the diagrams Fig. 7e and Fig. 7f for the individual specimens.

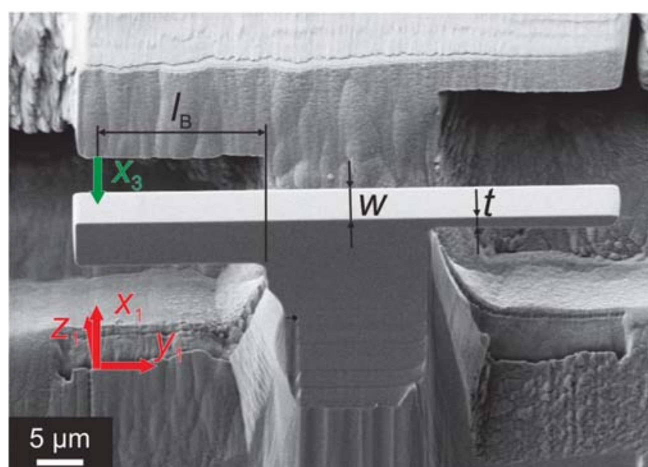

(a)

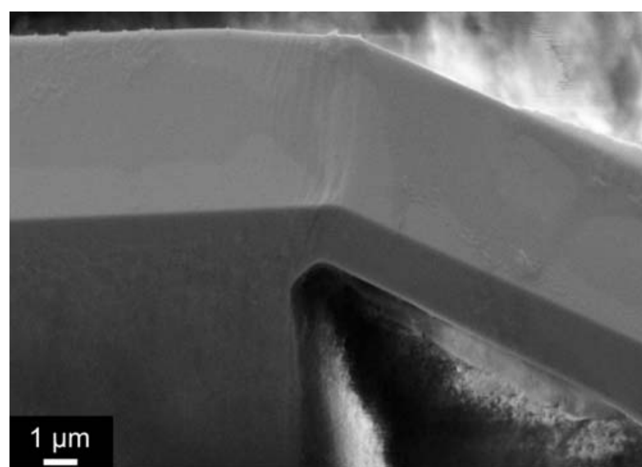

(b)

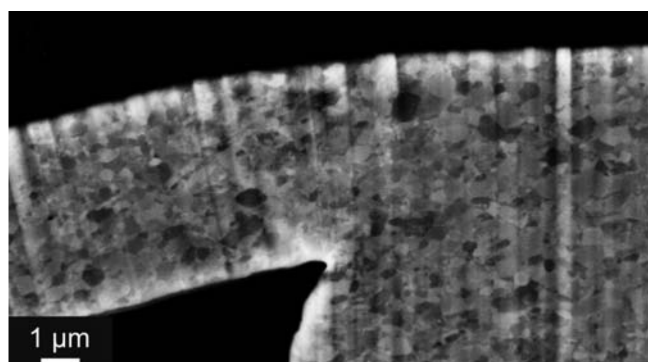

(c)

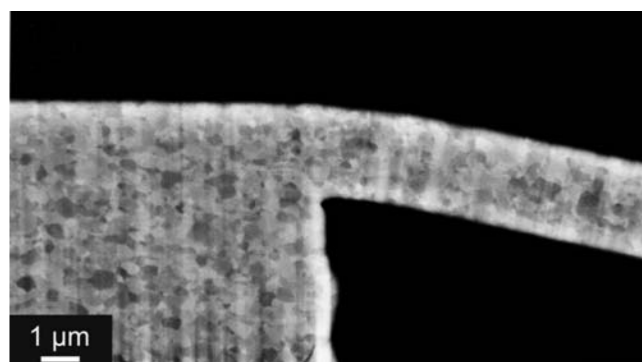

(d)

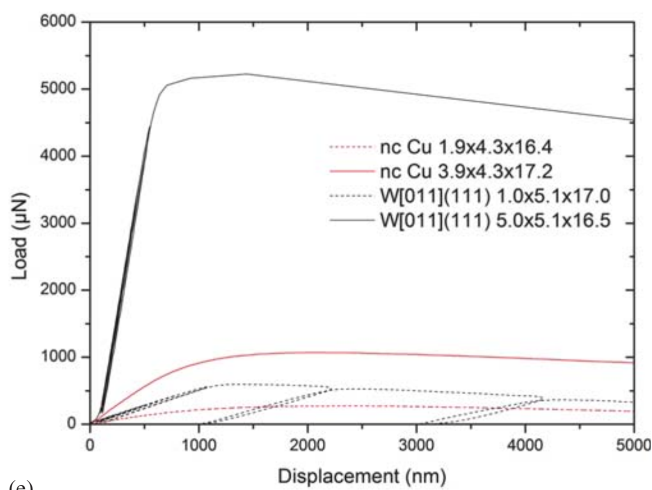

(e)

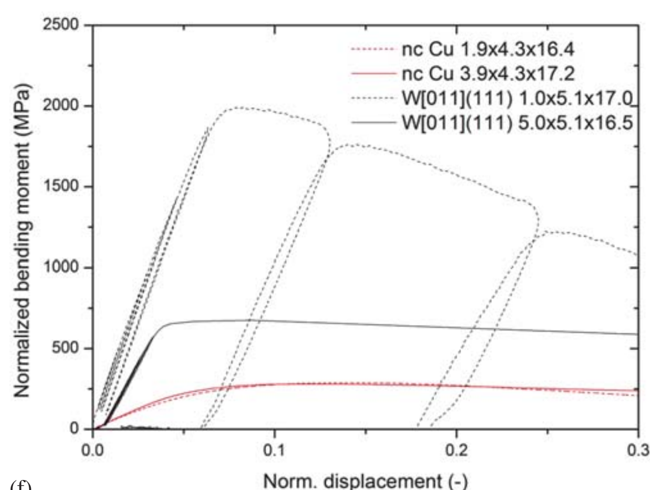

(f)

Fig. 7. (a) Inclined view of a FIB fabricated W[011](111) double bending beam with thicknesses of 5.0 µm and 1 µm, respectively. The width was 5 µm in both cases. (b) Inclined ex-situ SEM image showing glide steps on a deformed 1.0 µm thick W[011](111) bending beam. (c) Ex-situ backscatter electron image of a deformed 3.9 µm thick nanocrystalline Cu beam. (d) Ex-situ backscatter electron image of a 1.9 µm thick nanocrystalline Cu beam after bending. (e) Load versus displacement curves for four different bending beams. (f) Normalized bending moment $F \cdot l_B/(w \cdot t^2)$ versus normalized displacement u/l_B for the four presented bending beams. See text for details.

© 2009 Carl Hanser Verlag, Munich, Germany www.ijmr.de Not for use in internet or intranet sites. Not for electronic distribution.

For the single crystal W[110](111) samples a higher normalized flow stress (normalized bending moment) for the thinner sample is observed, as reported for single crystal Cu [27]. Considering the nanocrystalline Cu, there is no significant difference between the two specimens, although a higher strain gradient is present in the thinner sample. Again, with respect to the high defect density of this nanocrystalline material, no influence from FIB milling was expected and is not observed.

5.4. Bending fracture

Instead of pure bending of a beam, a defined notch can also be introduced by FIB milling to perform a bending fracture test as schematically shown in Fig. 8a. Figure 8b–d present images collected during the fracture test of a W single crystal. With increasing bending of the beam, the pre-crack grows. Also, the cube corner diamond tip slightly, but noticeably indents the W beam. During the test several intentional holding steps were conducted to record high quality SEM images required to precisely detect the actual crack length and deformation phenomena. These holding periods in the displacement controlled experiment manifest as significant load drops in the load versus displacement data (Fig. 8e). The positions corresponding to Fig. 8b–d are marked.

The most striking observation from the load versus displacement data and the in-situ images is the significant plastic deformation of the single crystal W fracture specimen, in contrast to bulk W which is known to fail by brittle fracture at room temperature [84, 85]. This remarkable amount of plasticity is clearly revealed by ex-situ backscat-

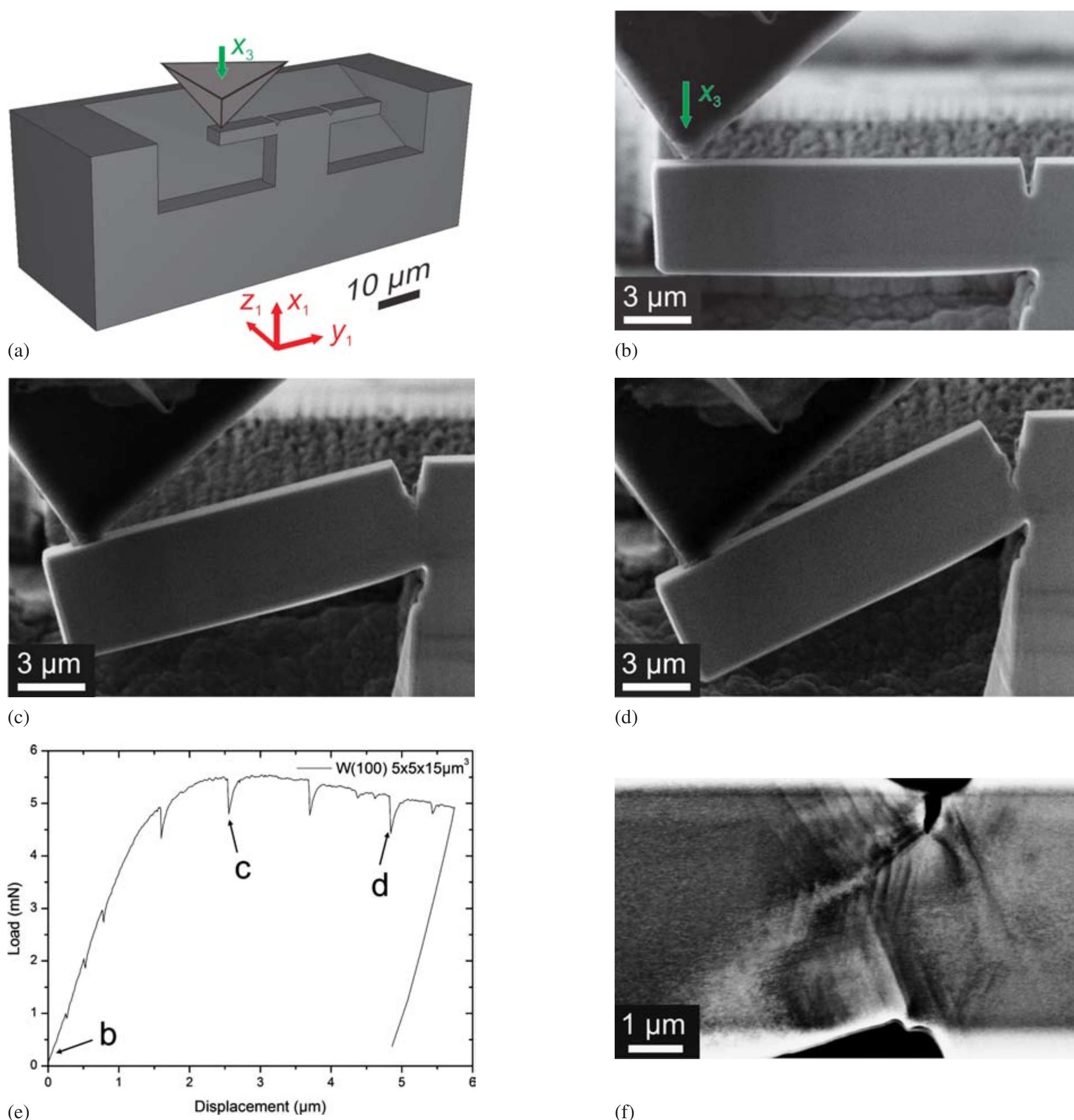

Fig. 8. (a) Schematic drawing of the fracture specimen FIB milled into the bulk W single crystal. (b–d) SEM images taken during loading to precisely evaluate the crack extension. (e) Load versus displacement curve of the fracture test. A remarkable amount of plastic deformation is observed. The positions along the loading path corresponding to Fig. 8b–d are indicated. (f) Ex-situ backscatter electron image showing the formation of slip lines along the crack path.

© 2009 Carl Hanser Verlag, Munich, Germany www.ijmr.de Not for use in internet or intranet sites. Not for electronic distribution.

ter electron investigation (Fig. 8f) showing the formation of slip steps adjacent to the crack path.

Since proper determination of any fracture mechanics characteristics requires knowledge of the actual crack length, in-situ observation is essential for this kind of testing. Finally, such types of experiments in conjunction with a variation in the size of the sample as well as the temperature will permit completely new insights to the fracture processes and the brittle to ductile transition regime.

5.5. Bending fatigue

In the previous examples, only unidirectional loading was applied. Fully reversed loading cannot be done by simple indentation, compression, or tension setups. But taking an indenter tip equipped with a side slit and well defined contact points in combination with a bending beam as depicted in Fig. 9a allows to bend the beam in $\pm x_1$ by actuating the indenter in $\pm x_3$. In the example provided in Fig. 9 the indenter was actuated displacement controlled with a sinusoidal displacement versus time curve at a frequency of $0.033\ s^{-1}$. 100 loading cycles were performed with amplitudes of ± 1 µm, ± 2 µm, ± 4 µm, and ± 8 µm each.

The subsequent in-situ SEM images in Fig. 9b–f show a single crystal single slip oriented Cu(–234) beam with dimensions of 3 µm × 3 µm × 50 µm in the aligned position before first loading with an amplitude of ± 1 µm (Fig. 9b). In Fig. 9c the sample is bent by +1 µm in the maximum upward position, while it is relaxed again in Fig. 9d. Figure 9e shows the sample deflected by – 1 µm in the chosen maximum downward position, while it is released after completing the first loading cycle in Fig. 9f. To bend the sample by a defined amount, the indenter has to be additionally actuated to compensate for the gap length l_{gap} = 6.8 µm between sample and wedges, as indicated in Fig. 9e. This gap is required to align sample and tip without previous deformation. Moreover, the use of a larger gap also allows testing of beams with larger dimensions using the same tip. The gap length is also indicated in the load versus displacement curve in Fig. 9g. After moving the tip without measuring any load, the wedge contacts the sample and bends it nearly elastically, as can be seen by the narrow hysteresis between loading and unloading portion. The position of the in-situ images is indicated along the loading path.

After cycling the sample a hundred times in the nearly elastic regime without indication of emerging slip steps in the in-situ SEM images, the bending amplitude was increased stepwise to ± 2 µm, ± 4 µm, and ± 8 µm for 100 cycles each. With increasing bending angle, increasing plasticity was observed. This is exemplarily shown in Fig. 10 for the second loading cycle at an amplitude of ± 2 µm. Figure 10a–d again shows the specimen in the unloaded, loaded, reverse loaded, and finally unloaded positions. Clear indication for one set of slip lines according to the single slip orientation is observed in the highly stressed region. The recorded load versus displacement curve in Fig. 10e shows, in contrast to the one given in Fig. 9, a broad hysteresis between loading and unloading part of the curve indicating a high amount of plastic deformation. The gap length is again indicated. Ex-situ SEM investigation of the fatigue specimen after cycling with amplitudes of ± 8 µm shows a high amount of fine slip traces and necking of the sample in the highly stressed region close to the base. A detailed analysis of these fatigue experiments will be described in a forthcoming publication [86].

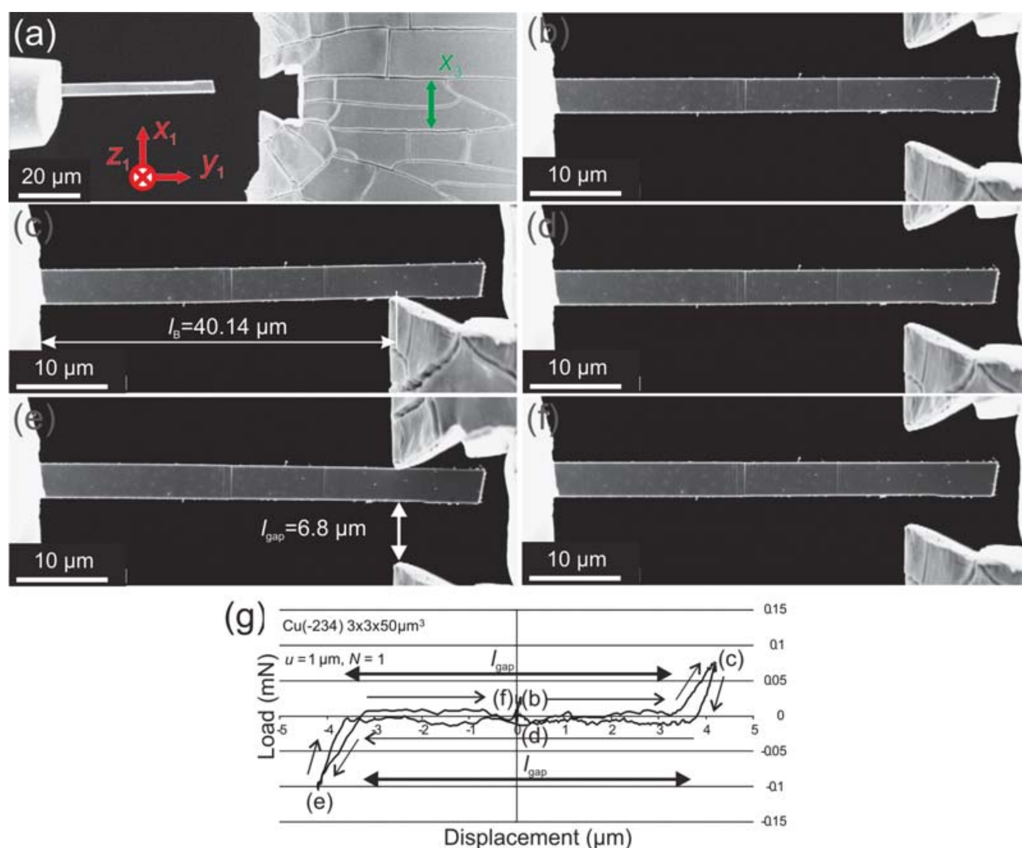

Fig. 9. (a) Low magnification overview of the bending fatigue setup with a single crystal Cu(–234) sample with dimensions of 3 µm × 3 µm × 50 µm and a tungsten holder with FIB cut edges during alignment. (b–f) Subsequent in-situ SEM images showing the sample in the first loading cycle with an amplitude of ± 1 µm: Before loading (b), at maximum upward bending displacement of +1 µm (c), after unloading in neutral position (d), at maximum downward bending displacement of – 1 µm (e), and after the loading cycle in neutral position (f). (g) Recorded load versus displacement curve of the bending cycle depicted above showing nearly elastic behavior. The positions of images (b–f) along the loading path are indicated. The gap length of l_{gap} = 6.8 µm is shown in (e) and indicated in (g), the bending length of l_B = 40.14 µm is indicated in (c).

© 2009 Carl Hanser Verlag, Munich, Germany www.ijmr.de Not for use in internet or intranet sites. Not for electronic distribution.

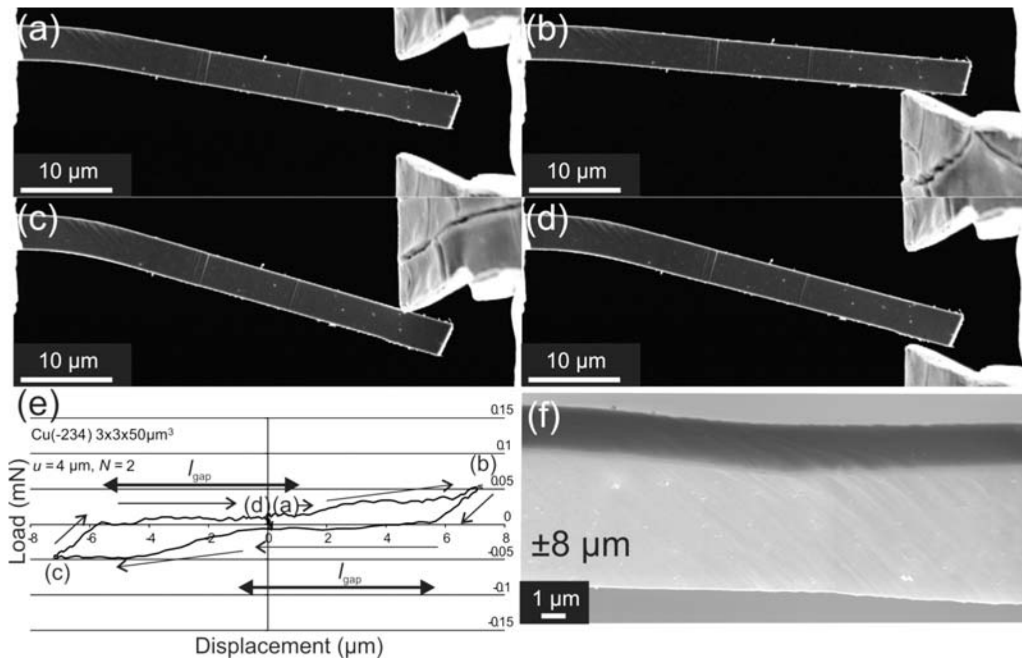

Fig. 10. (a–d) In-situ SEM images showing the same specimen as in Fig. 9 during the second loading cycle with an amplitude of ±4 μm after having sustained 100 loading cycles with amplitudes of ±1 μm and ±2 μm: Before loading (a), at maximum upward bending displacement of +4 μm (b), at maximum downward bending displacement of −4 μm (c), and after the loading cycle in neutral position (d). Note the clearly visible slip steps in the highly stressed region. (e) Recorded load versus displacement curve of the bending cycle depicted above showing clearly plastic behavior. The positions of images (a–d) along the loading path are indicated. (f) Inclined ex-situ SEM image showing the fatigue sample after it was additionally cycled 100 times with even higher amplitudes of ±8 μm. A large number of fine slip steps as well as indication of necking are observed.

6. Further complementary methods and outlook

Simple monitoring during an in-situ SEM test provides reliable alignment [48, 49] in conjunction with valuable insights with respect to, for example, the deformation mode [52], the acting slip system [34], and the failure mode [22]. However, there are several other analysis techniques available when using in-situ SEM tests.

6.1. Image correlation

Obviously, the images recorded during the in-situ test can be used for subsequent analysis. For example, by comparing subsequent SEM images taken during in-situ straining, a precise measure of the global sample strain as well as the strain localization on the sample surface can be determined [87, 88]. The group of Michler [22] facilitated real-time image correlation techniques to improve the accuracy of their strain measurement. Moreover, the sample sink-in [16, 18, 29, 48], a common problem in micro-compression testing for samples that are not situated on a rigid substrate [32, 74, 89], can be analyzed and compared to analytical solutions [90].

To further illustrate this issue, a grid with ~1 μm spacing was written on a single crystal Cu(100) sample with dimensions of 8 μm × 8 μm × 12 μm using the FIB with a Ga^+ ion current of 20 pA (Fig. 11a). This mesh was discretized and is plotted in the uncompressed state (red) and after compression of Δx_3 = 1 μm (blue) in Fig. 11b. Besides movement of the flat punch and displacement of the mesh positions in the upper half of the pillar, noticeable deformation is seen below the sample base. Subsequent snapshots of the deformed grid after compression by Δx_3 = 2 μm and Δx_3 = 3 μm in comparison with the previous state after compression by Δx_3 = 1 μm and Δx_3 = 2 μm are shown in Fig. 11c and Fig. 11d, respectively. As can be seen by the detail taken from Fig. 11c shown in Fig. 11e, the deformation of the sample base is not homogeneous, but resembles similarities to the slip line field (also known as Prandtl field).

Evaluating the average sample displacement at the base position indicated in Fig. 11e leads to sample sink-in displacements of 234 ± 15 nm for displacements from 0 μm to 1 μm in Fig. 11b, 188 ± 56 nm for displacements from 1 μm to 2 μm in Fig. 11c, and 217 ± 50 nm for displacements from 2 μm to 3 μm in Fig. 11d. In contrast, the analytical Sneddon solution [90] predicts 113 nm, 23 nm, and 27 nm, respectively. These significant differences can be rationalized by considering some facts. First Sneddon derived this solution for a semi-infinite halfspace penetrated by a cylindrical punch. Common sample geometries deviate from this idealized geometry and will behave more softly [48]. This is especially the case for the sample shown, since for viewing purposes the base had to be partially removed, thus resembling more closely a "half-half-space". This is only the case for this compression test, but was not the usual sample configuration. Second, there is a not negligible amount of plastic deformation taking place beneath the sample base, leading to hardening of the base material, as reported previously [29]. Thus, the sample behaves as having a larger effective diameter.

Besides correcting for experimental uncertainties, such image correlation techniques can also be applied to determine the local strain distribution on the sample surface [87, 91]. Figure 11f shows an overlay between one of the cross-correlated in-situ SEM images and the corresponding local deformation map showing the ε_{xx} component of the strain field obtained using MeX 4.0 software (Alicona Imaging GmbH, Krambach, Austria). While the global compressive strain determined from the load versus displace-

© 2009 Carl Hanser Verlag, Munich, Germany www.ijmr.de Not for use in internet or intranet sites. Not for electronic distribution.

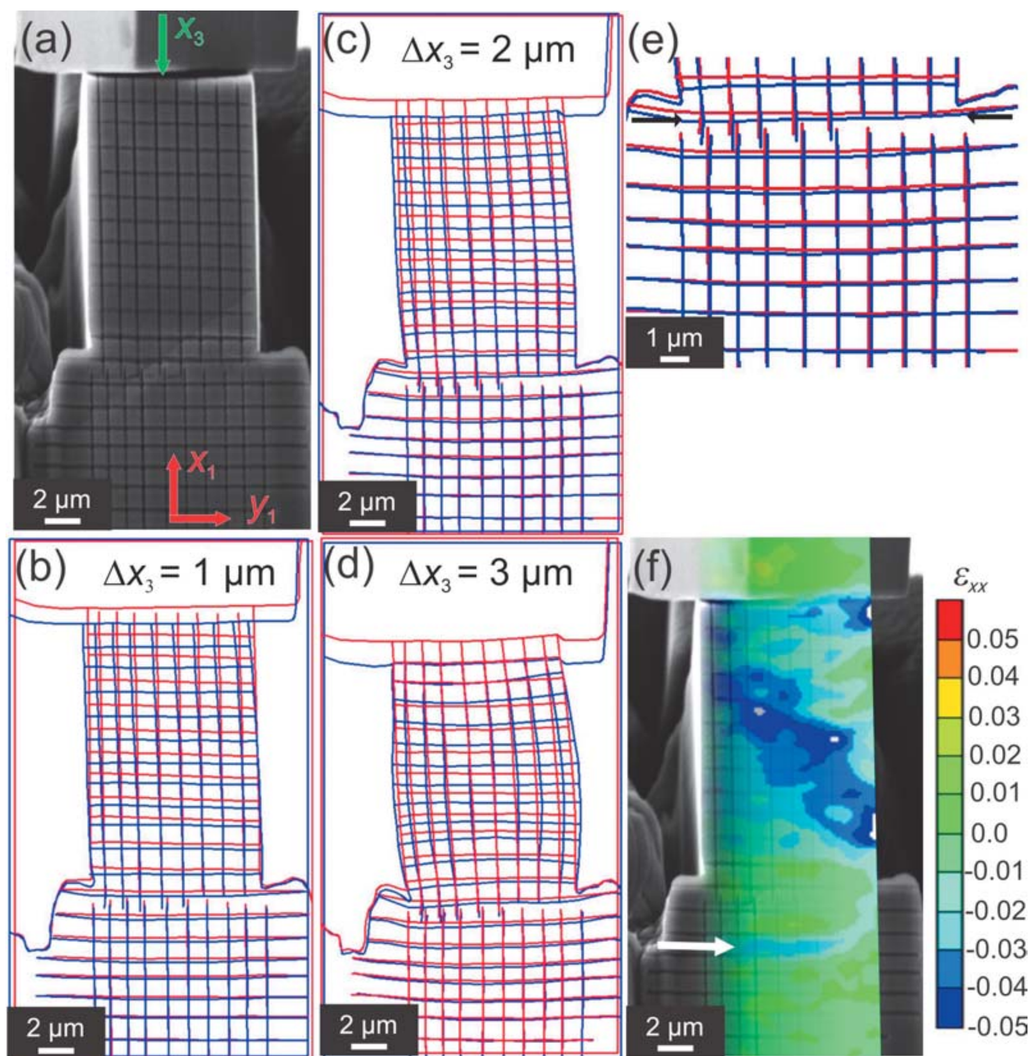

Fig. 11. (a) 8 µm × 8 µm × 12 µm single crystal Cu(100) compression sample with a FIB made grid having ~1 µm spacing. (b) Overlay of the discretized meshes of the unloaded sample (red) and after Δx_3 = 1 µm compression (blue). (c) Comparison of the mesh after Δx_3 = 1 µm (red) and Δx_3 = 2 µm (blue) deformation. (d) The deformed grid at Δx_3 = 2 µm (red) and Δx_3 = 3 µm (blue) compression. (e) Detail of the deformed sample base from (c). (f) Overlay between in-situ SEM image and the corresponding local strain mapping showing the ε_{xx} strain component. Strain along the expected 45° inclined slip plane, at the sample top, and sink-in at the sample base (arrow) were observed.

© 2009 Carl Hanser Verlag, Munich, Germany www.ijmr.de Not for use in internet or intranet sites. Not for electronic distribution.

ment curve was 0.06 between the two images, only at white spots in Fig. 11f a compressive strain higher than 0.05 was reached. Compressive strains of ~0.05 are observed at an inclination of ~45° corresponding to the expected slip plane. This is of special interest, since this allows determining strain localization and active slip systems even before slip steps are observed in the in-situ images. Moreover, again localized deformation at the sample top is shown [34, 60]. In accordance with the previous discussion, the image cross-correlation also shows a significant amount of deformation beneath the sample base, as indicated by an arrow in Fig. 11f.

6.2. Electron backscatter diffraction

In-situ SEM images show the actual deformation of the samples with the active slip systems, which can be extended as shown above by post image correlation techniques. A striking feature of in-situ micro-Laue techniques [59, 60] is the capability to locally monitor changes in the crystallographic structure of the sample during testing. While micro-Laue requires use of a synchrotron beamline, similar information can be gained using electron backscatter diffraction (EBSD) techniques in an SEM [92]. It has already been shown that the data gained by in-situ micro-Laue X-ray diffraction and ex-situ EBSD investigation of the identical micrometer sized single crystal specimen [60, 93] are in excellent agreement and complement each other with respect to lateral and angular resolution. While ex-situ EBSD has been demonstrated for miniaturized compression [34, 60], bending [27], and tensile [28, 93] samples, in-situ EBSD requires tilting of the whole testing setup by typically 65°–

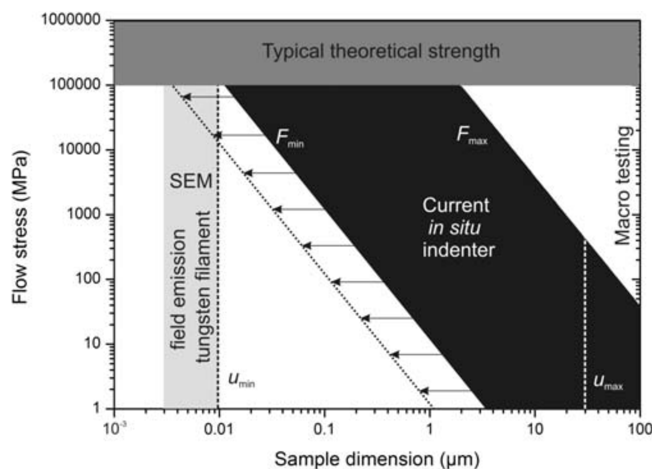

Fig. 12. Application window for the existing in-situ SEM indenter used in this study as a function of sample dimension and flow stress of the material. Possible extension towards nanomechanics by using a more sensitive load cell is indicated by arrows.

70° around t_1 (see Fig. 2). Therefore, to load the sample without blocking the electron beam, the indenter needs to be mounted on the back of the SEM chamber to align the x_3 direction with the y_2 direction (Fig. 2). This is not possible for the present SEM chamber, since no flange exists at this position, but can be realized when designing a new setup.

7. Towards in-situ nanomechanics in an SEM

Through the foregoing examples it was shown that, with the exception of torsional loading, all common mechanical testing techniques have been successfully downscaled to the micrometer regime by the combination of a FIB workstation for fabrication issues and the use of a single indenter system equipped with various custom tips and installed in an SEM for in-situ loading of the samples. This unique combination offers large flexibility in combination with a minimum amount of instruments, thus being very efficient.

However, as for any setup, there is a typical application window, as shown in Fig. 12, given by the load and displacement range of the setup in conjunction with the flow stress and dimensions of the sample to be tested. In our present case, the maximum load is 300 mN and the maximum displacement 30 μm. The lower limits are given by the experimental noise, which is below 10 μN (see for example Fig. 10e) and better than ±5 nm for the indenter mounted in the SEM without sample contact. This is also about the resolution provided by the SEM used. This allows covering a large area of what is commonly attributed to as micro-mechanics.

Moreover, there is no principal restriction to extending these techniques into the nanometer regime. FIB fabrication of samples with dimensions of several tens of nanometers can be achieved. However, the increasing fraction of FIB modified material surface (ion damage) with respect to the total tested volume might set a limit to this fabrication method [63]. Nevertheless, there is a growing field of nanomaterials including nanowires and whiskers where mechanical properties need to be determined. Load cells with a compact design and higher resolution to extend testing towards lower loads have become commercially available [53, 94]. The possible extension of the operation window using such load cells is indicated by arrows in Fig. 12. The compact design reduces the masses in the SEM chamber that need to be actively damped and allows operating at a lower working distance in the SEM, thus gaining better resolution. Finally, using a field emission SEM or a dual beam FIB workstation as an all-in-one tool increases the imaging resolution for reliable strain determination of nanometer sized samples.

The authors thank Dr. Thomas Chudoba and his co-workers for the excellent support during hardware and software adaptation of the in-situ micro-indenter in order to meet the special requirements for the performed work. Partial financial support by the Austrian Fonds zur Förderung der wissenschaftlichen Forschung, Project P17375-N07, and within the research activities of the K2 Competence Centre on "Integrated Research in Materials, Processing and Product Engineering", operated by the Materials Center Leoben Forschung GmbH under the frame of the Austrian COMET Competence Centre Program, is acknowledged. D.K. gratefully acknowledges financial support by the Austrian Science Fund (FWF) through the Erwin Schrödinger scholarship J2834-N20.

© 2009 Carl Hanser Verlag, Munich, Germany www.ijmr.de Not for use in internet or intranet sites. Not for electronic distribution.

References

[1] E.O. Hall: Proc. Phys. Soc. Lond. B 64 (1951) 747.
[2] N.J. Petch: J. Iron Steel 174 (1953) 25.
[3] E. Arzt: Acta Mater. 46 (1998) 5611. DOI:10.1016/S1359-6454(98)00231-6
[4] J.S. Stölken, A.G. Evans: Acta Mater. 46 (1998) 5109. DOI:10.1016/S1359-6454(98)00153-0
[5] N.A. Fleck, G.M. Muller, M.F. Ashby, J.W. Hutchinson: Acta Met. Mater. 42 (1994) 475. DOI:10.1016/0956-7151(94)90502-9
[6] N.A. Stelmashenko, M.G. Walls, L.M. Brown, Y.V. Milman: Acta Met. Mater. 41 (1993) 2855. DOI:10.1016/0956-7151(93)90100-7
[7] W.D. Nix, H. Gao: J. Mech. Phys. Solids 46 (1998) 411. DOI:10.1016/S0022-5096(97)00086-0
[8] M.A. Haque, M.T.A. Saif: Experim. Mech. 43 (2003) 248. DOI:10.1007/BF02410523
[9] A.M. Minor, S.A.S. Asif, Z.W. Shan, E.A. Stach, E. Cyrankowski, T.J. Wyrobek, O.L. Warren: Nat. Mater. 5 (2006) 697. DOI:10.1038/nmat1714
10] M.J. Cordill, M.D. Chambers, M.S. Lund, D.M. Hallman, C.R. Perrey, C.B. Carter, A. Bapat, U. Kortshagen, W.W. Gerberich: Acta Mater. 54 (2006) 4515. DOI:10.1016/j.actamat.2006.05.037
[11] P.A. Gruber, C. Solenthaler, E. Arzt, R. Spolenak: Acta Mater. 56 (2008) 1876. DOI:10.1016/j.actamat.2007.12.043
[12] M.W. Phaneuf: Micron 30 (1999) 277. DOI:10.1016/S0968-4328(99)00012-8
[13] M.D. Uchic, D.M. Dimiduk, J.N. Florando, W.D. Nix: Science 305 (2004) 986. DOI:10.1126/science.1098993
[14] D.M. Dimiduk, M.D. Uchic, T.A. Parthasarathy: Acta Mater. 53 (2005) 4065. DOI:10.1016/j.actamat.2005.05.023
[15] M.D. Uchic, D.M. Dimiduk: Mater. Sci. Eng. A 400–401 (2005) 268. DOI:10.1016/j.msea.2005.03.082
[16] J.R. Greer, W.C. Oliver, W.D. Nix: Acta Mater. 53 (2005) 1821. DOI:10.1016/j.actamat.2004.12.031
[17] J.R. Greer, W.C. Oliver, W.D. Nix: Acta Mater. 54 (2006) 1705 [Corrigendum]. DOI:10.1016/j.actamat.2005.12.004
[18] C.A. Volkert, E.T. Lilleodden: Phil. Mag. 86 (2006) 5567. DOI:10.1080/14786430600567739
[19] R. Maaß, D. Grolimund, S. Van Petegem, M. Willimann, M. Jensen, H. Van Swygenhoven, T. Lehnert, M.A.M. Gijs, C.A. Volkert, E.T. Lilleodden, R. Schwaiger: App. Phys. Lett. 89 (2006) 151905. DOI:10.1063/1.2358204
[20] D. Kiener, C. Motz, T. Schöberl, M. Jenko, G. Dehm: Adv. Eng. Mater. 8 (2006) 1119. DOI:10.1002/adem.200600129
[21] J. Michler, K. Wasmer, S. Meier, F. Ostlund, K. Leifer: App. Phys. Lett. 90 (2007) 043123. DOI:10.1063/1.2432277
[22] B. Moser, K. Wasmer, L. Barbieri, J. Michler: J. Mater. Res. 22 (2007) 1004. DOI:10.1557/JMR.2007.0140
[23] C.P. Frick, S. Orso, E. Arzt: Acta Mater. 55 (2007) 3845. DOI:10.1016/j.actamat.2007.02.034
[24] K.S. Ng, A.H.W. Ngan: Acta Mater. 56 (2008) 1412. DOI:10.1016/j.actamat.2007.12.016
[25] Z.W. Shan, R.K. Mishra, S.A.S. Asif, O.L. Warren, A.M. Minor: Nat. Mater. 73 (2008) 115. DOI:10.1038/nmat2085
[26] B.E. Schuster, Q. Wei, T.C. Hufnagel, K.T. Ramesh: Acta Mater. 56 (2008) 5091. DOI:10.1016/j.actamat.2008.06.028
[27] C. Motz, T. Schöberl, R. Pippan: Acta Mater. 53 (2005) 4269. DOI:10.1016/j.actamat.2005.05.036
[28] D. Kiener, W. Grosinger, G. Dehm, R. Pippan: Acta Mater. 56 (2008) 580. DOI:10.1016/j.actamat.2007.10.015
[29] C.P. Frick, B.G. Clark, S. Orso, A.S. Schneider, E. Arzt: Mater. Sci. Eng. A 489 (2008) 319. DOI:10.1016/j.msea.2007.12.038
[30] D.M. Dimiduk, C. Woodward, R. LeSar, M.D. Uchic: Science 312 (2006) 1188. DOI:10.1126/science.1123889
[31] F.F. Csikor, C. Motz, D. Weygand, M. Zaiser, S. Zapperi: Science 318 (2007) 251. DOI:10.1126/science.1143719
[32] D. Kiener, C. Motz, G. Dehm: Mater. Sci. Eng. A 505 (2009) 79. DOI:10.1016/j.msea.2009.01.005
[33] O.L. Warren, S.A. Downs, T.J. Wyrobek: Z. Metallkd. 95 (2004) 287. http://www.ijmr.de/directlink.asp?MK017951
[34] D. Kiener, C. Motz, G. Dehm: J. Mater. Sci. 43 (2008) 2503. DOI:10.1007/s10853-008-2531-3
[35] D. Kiener, W. Grosinger, G. Dehm: Scripta Mater. 60 (2009) 148. DOI:10.1016/j.scriptamat.2008.09.024
[36] J.R. Greer, C.R. Weinberger, W. Cai: Mater. Sci. Eng. A 493 (2008) 21. DOI:10.1016/j.msea.2007.08.093
[37] R. Dou, B. Derby: Scripta Mater. In Press, Accepted Manuscript). DOI:10.1016/j.scriptamat.2009.05.012

© 2009 Carl Hanser Verlag, Munich, Germany www.ijmr.de Not for use in internet or intranet sites. Not for electronic distribution.

[38] T.A. Parthasarathy, S.I. Rao, D.M. Dimiduk, M.D. Uchic, D.R. Trinkle: Scripta Mater. 56 (2007) 313. DOI:10.1016/j.scriptamat.2006.09.016
[39] S.I. Rao, D.M. Dimiduk, M. Tang, T.A. Parthasarathy, M.D. Uchic, C. Woodward: Phil. Mag. 87 (2007) 4777. DOI:10.1080/14786430701591513
[40] B. von Blanckenhagen, E. Arzt, P. Gumbsch: Acta Mater. 52 (2004) 773. DOI:10.1016/j.actamat.2003.10.022
[41] J.A. El-Awady, M. Wen, N.M. Ghoniem: J. Mech. Phys. Solids 57 (2009) 32. DOI:10.1016/j.jmps.2008.10.004
[42] S.H. Oh, M. Legros, D. Kiener, G. Dehm: Nat. Mater. 8 (2009) 95. DOI:10.1038/nmat2370
[43] S.I. Rao, D.M. Dimiduk, T.A. Parthasarathy, M.D. Uchic, M. Tang, C. Woodward: Acta Mater. 56 (2008) 3245. DOI:10.1016/j.actamat.2008.03.011
[44] A.S. Schneider, B.G. Clark, C.P. Frick, P.A. Gruber, E. Arzt: Mater. Sci. Eng. A 508 (2009) 241. DOI:10.1016/j.msea.2009.01.011
[45] P.J. Guruprasad, A.A. Benzerga: J. Mech. Phys. Solids 56 (2008) 132. DOI:10.1016/j.jmps.2007.03.009
[46] S. Buzzi, M. Dietiker, K. Kunze, R. Spolenak, J.F. Loffler: Phil. Mag. 89 (2009) 869. DOI:10.1080/14786430902791748
[47] M.D. Uchic, P.A. Shade, D. Dimiduk: Ann. Rev. Mater. Res. 39 (2009). DOI:10.1146/annurev-matsci-082908-145422
[48] H. Zhang, B.E. Schuster, Q. Wei, K.T. Ramesh: Scripta Mater. 54 (2006) 181. DOI:10.1016/j.scriptamat.2005.06.043
[49] Y.S. Choi, M.D. Uchic, T.A. Parthasarathy, D.M. Dimiduk: Scripta Mater. 57 (2007) 849. DOI:10.1016/j.scriptamat.2007.06.057
[50] M.D. Uchic, D.M. Dimiduk, R. Wheeler, P.A. Shade, H.L. Fraser: Scripta Mater. 54 (2006) 759. DOI:10.1016/j.scriptamat.2005.11.016
[51] R. Rabe, J.M. Breguet, P. Schwaller, S. Stauss, F.J. Haug, J. Patscheider, J. Michler: Thin Solid Films 469-470 (2004). DOI:10.1016/j.tsf.2004.08.096
[52] B. Moser, J.F. Loffler, J. Michler: Phil. Mag. A 86 (2006) 5715. DOI:10.1080/14786430600627301
[53] K.A. Rzepiejewska-Malyska, G. Buerki, J. Michler, R.C. Major, E. Cyrankowski, S.A.S. Asif, O.L. Warren: J. Mater. Res. 23 (2008) 1973. DOI:10.1557/jmr.2008.0240
[54] K. Svensson, Y. Jompol, H. Olin, E. Olsson: Rev. Sci. Instrum. 74 (2003) 4945. DOI:10.1063/1.1614872
[55] M.S. Bobji, C.S. Ramanujan, J.B. Pethica, B.J. Inkson: Meas. Sci. Technol. 17 (2006) 1324. DOI:10.1088/0957-0233/17/6/006
[56] I.M. Robertson, P.J. Ferreira, G. Dehm, R. Hull, E.A. Stach: MRS Bull. 33 (2008) 122.
[57] J. Ye, R.K. Mishra, A.M. Minor: Scripta Mater. 59 (2008) 951. DOI:10.1016/j.scriptamat.2008.06.052
[58] R. Maaß, S.V. Petegem, J. Zimmermann, C.N. Borca, H.V. Swygenhoven: Scripta Mater. 59 (2008) 471. DOI:10.1016/j.scriptamat.2008.04.034
[59] R. Maaß, S. Van Petegem, H. Van Swygenhoven, P.M. Derlet, C.A. Volkert, D. Grolimund: Phys. Rev. Lett. 99 (2007) 145505. DOI:10.1103/PhysRevLett.99.145505
[60] R. Maaß, S. Van Petegem, D. Grolimund, H. Van Swygenhoven, D. Kiener, G. Dehm: App. Phys. Lett. 92 (2008) 071905. DOI:10.1063/1.2884688
[61] K. Wasmer, T. Wermelinger, A. Bidiville, R. Spolenak, J. Michler: J. Mater. Res. 23 (2008) 3040. DOI:10.1557/jmr.2008.0363
[62] H. Bei, S. Shim, G.M. Pharr, E.P. George: Acta Mater. 56 (2008) 4762. DOI:10.1016/j.actamat.2008.05.030
[63] D. Kiener, C. Motz, M. Rester, G. Dehm: Mater. Sci. Eng. A 459 (2007) 262. DOI:10.1016/j.msea.2007.01.046
[64] L.A. Giannuzzi, F.A. Stevie: Introduction to focused ion beams, Springer, New York (2005).
[65] C.A. Volkert, A.M. Minor: MRS Bull. 32 (2007) 389.
[66] H. Bei, S. Shim, E.P. George, M.K. Miller, E.G. Herbert, G.M. Pharr: Scripta Mater. 57 (2007) 397. DOI:10.1016/j.scriptamat.2007.05.010
[67] S. Shim, H. Bei, M.K. Miller, G.M. Pharr, E.P. George: Acta Mater. 57 (2009) 503. DOI:10.1016/j.actamat.2008.09.033
[68] H. Bei, S. Shim, M.K. Miller, G.M. Pharr, E.P. George: App. Phys. Lett. 91 (2007) 111915. DOI:10.1063/1.2784948
[69] J. Marien, J.M. Plitzko, R. Spolenak, R.-M. Keller, J. Mayer: J. Microscopy 194 (1999) 71.
[70] S. Schmidt, W. Sigle, W. Gust, M. Rühle: Z. Metallkd. 93 (2002) 428. http://www.ijmr.de/directlink.asp?MK020428
[71] W. Sigle, G. Richter, M. Ruhle, S. Schmidt: App. Phys. Lett. 89 (2006) 121911. DOI:10.1063/1.2356322
[72] T. Chudoba, P. Schwaller, R. Rabe, J.M. Breguet, J. Michler: Phil. Mag. A 86 (2006) 5265. DOI:10.1080/14786430600746424
[73] S. Wurster, R. Pippan: Scripta Mater. 60 (2009) 1083. DOI:10.1016/j.scriptamat.2009.01.011
[74] H. Wörgötter, D. Kiener, J.M. Purswani, D. Gall, G. Dehm: Berg- und Hüttenmännische Monatshefte 153 (2008) 257. DOI:10.1007/s00501-008-0386-1
[75] D. Tabor: Sheet Met. Ind. 31 (1954) 749.
[76] D.M. Marsh: Proc. R. Soc. Lond. A 279 (1964) 420. DOI:10.1098/rspa.1964.0114
[77] P. Hosemann, J.G. Swadener, D. Kiener, G.S. Was, S.A. Maloy, N. Li: J. Nuc. Mater. 375 (2008) 135. DOI:10.1016/j.jnucmat.2007.11.004
[78] R. Pippan, F. Wetscher, M. Hafok, A. Vorhauer, I. Sabirov: Adv. Eng. Mater. 8 (2006) 1046. DOI:10.1002/adem.200600133
[79] D. Kiener, M. Rester, S. Scheriau, B. Yang, R. Pippan, G. Dehm: Int. J. Mat. Res. 98 (2007) 1047. DOI:10.3139/146.101578
[80] G. Khatibi, A. Betzwar-Kotas, V. Gröger, B. Weiss: Fatigue Fract. Eng. Mater. Struct. 28 (2005) 723. DOI:10.1111/j.1460-2695.2005.00898.x
[81] B. Yang, C. Motz, W. Grosinger, W. Kammrath, G. Dehm: Int. J. Mat. Res. 99 (2008) 716. DOI:10.3139/146.101690
[82] K.S. Ng, A.H.W. Ngan: Scripta Mater. 59 (2008) 796. DOI:10.1016/j.scriptamat.2008.06.019
[83] C. Motz, D. Weygand, J. Senger, P. Gumbsch: Acta Mater. 56 (2008) 1942. DOI:10.1016/j.actamat.2007.12.053
[84] P. Gumbsch: J. Nuc. Mater. 323 (2003) 304. DOI:10.1016/j.jnucmat.2003.08.009
[85] M. Faleschini, H. Kreuzer, D. Kiener, R. Pippan: J. Nuc. Mater. 367–370 (2007) 800. DOI:10.1016/j.jnucmat.2007.03.079
[86] D. Kiener, C. Motz, D. Weygand, R. Pippan: under prep. (2009).
[87] A. Tatschl, O. Kolednik: Mater. Sci. Eng. A 339 (2003) 265. DOI:10.1016/S0921-5093(02)00111-9
[88] A. Tatschl, C. Motz, R. Pippan, O. Kolednik, in: T.W. Clyne, F. Simancik (Eds.), The Characterization of Crystal Plasticity by Orientation Image Microscopy and Local Deformation Measurements. Metal Matrix Composites and Metallic Foams. 2005. p. 151.
[89] A.S. Budiman, S.M. Han, J.R. Greer, N. Tamura, J.R. Patel, W.D. Nix: Acta Mater. 56 (2008) 602. DOI:10.1016/j.actamat.2007.10.031
[90] I.N. Sneddon: Int. J. Eng. Sci. 3 (1965) 47. DOI:10.1016/0020-7225(65)90019-4
[91] O. Kolednik: Adv. Eng. Mater. 8 (2006) 1079. DOI:10.1002/adem.200600150
[92] V. Randle, O. Engler: Introduction to Texture Analysis: macrotexture, microtexture and orientation mapping, Gordon & Breach, Amsterdam (2000).
[93] C. Kirchlechner, D. Kiener, N. Vaxelaire, J.-S. Micha, O. Ulrich, O. Thomas, G. Dehm, J. Keckes: under prep. (2009).
[94] D.S. Gianola, C. Eberl: JOM 61 (2009) 24. DOI:10.1007/s11837-009-0037-3

(Received January 19, 2009; accepted June 3, 2009)

Bibliography

DOI 10.3139/146.110149
Int. J. Mat. Res. (formerly Z. Metallkd.)
100 (2009) 8; page 1074–1087
© Carl Hanser Verlag GmbH & Co. KG
ISSN 1862-5282

Correspondence address

Dr. Daniel Kiener
National Center for Electron Microscopy
Lawrence Berkeley National Laboratory
One Cyclotron Road, MS 72-150, Berkeley, CA 94720, U.S.A.
Tel.: +1 510 486 4614
Fax: +1 510 486 5888
E-mail: dkiener@lbl.gov

You will find the article and additional material by entering the document number **MK110149** on our website at *www.ijmr.de*